An Equalized ADMM-Based High-Resolution Autofocusing Imaging Algorithm for THz-SAR Ground Moving Targets

Xiaoyu Qin, Bin Deng, Hongqiang Wang, Yang Zeng, Xu Chen, and Han Xiao

***Abstract*—Terahertz (THz) radar is well-suited for dynamic mobile target surveillance due to its high frame rates, minimal delay, and superior resolution. However, the defocusing problem caused by the motion of targets in the scene and the nonideal motion of the airborne platform severely affect synthetic aperture radar (SAR) imaging, particularly in the THz wave band. To address this issue, this article proposes a high-resolution imaging algorithm for THz-SAR ground-moving targets using the equalized alternating direction method of multipliers (ADMM). First, the range-Doppler algorithm is employed to generate a coarse image and extract the moving target region as the region of interest. Then, the range profile can be obtained by applying the inverse, which serves as input for the ADMM solving algorithm. Finally, the 2-D image of the target is reconstructed iteratively. The algorithm fully exploits the low-rank and sparse characteristics of moving targets in the SAR image to separate them from the background. It updates the azimuthal matched filter iteratively by minimizing image entropy and designs the equalization factor to retain target details while maintaining image sparsity. This approach significantly improves focusing accuracy compared with conventional algorithms while maintaining high imaging speed without estimating Doppler parameters.**

***Index Terms*—Alternating direction method of multipliers (ADMM), moving target imaging, regularization optimization, synthetic aperture radar (SAR), terahertz (THz).**

I. Introduction

SYNTHETIC aperture radar (SAR) is a microwave remote sensing technology proposed by Wiley in the 1950s. It actively transmits electromagnetic waves, receives echo data, and derives target scattering information through signal processing. Microwave remote sensing offers the advantages of prolonged distance detection, all-day and all-weather [1]. However, with its low frame rate, high delay, and other factors, conventional microwave band SAR imaging falls short of meeting the demands of dynamic monitoring for mobile targets. In contrast, the utilization of high frame rate Teraherz-SAR (THz-SAR) enables real-time monitoring and precise imaging of moving targets, facilitating accurate localization, and dynamic tracking. This technology finds extensive application across various sectors, spanning civilian, defense, and military fields [2]. In military contexts, particularly within tactical reconnaissance, THz-SAR imaging of moving targets assumes a pivotal role in battlefield surveillance. There are numerous moving targets on the battlefield, including combat vehicles, tanks, warships, and so on. Information gleaned from these moving targets can provide a further foundation for military decision-making. In civilian applications, THz-SAR performs well in continuous climate monitoring, terrain mapping, and ocean surveillance throughout the day. Meanwhile, it can detect the movement of vehicles on land and ships at sea in actual time. This capability provides indispensable control information for traffic control.

However, when employing classical imaging algorithms in the presence of target motion within the scene, it will inevitably result in the noncoherent accumulation of the moving target, giving rise to issues, such as defocusing and low-resolution problems in SAR imaging, even deviating from the actual target position, highlighting the inherent challenges in imaging moving targets compared with their static counterparts [3]. Consequently, there is an urgent demand to explore methods specifically tailored to achieve high-resolution imaging of moving targets.

Despite the considerable attention given to detecting moving targets from SAR images over the past decades, previous studies have predominantly concentrated on the detection of such targets. Because of the low resolution inherent in the original SAR images, most of the moving targets in these images generally manifest as mere points, hindering the extraction of details of themselves. Therefore, achieving high-resolution imaging of moving targets in the THz-SAR regime remains a challenging endeavor.

Several approaches have been proposed in recent years to address the moving target's refocusing problem in SAR images. These approaches can be divided into two categories, one is the traditional method based on motion compensation and the

Manuscript received 14 January 2024; revised 26 February 2024; accepted 1 April 2024. Date of publication 10 April 2024; date of current version 22 April 2024. This work was supported in part by the National Key Research and Development Program of China under Grant 2022YFB3902400 and in part by the National Natural Science Foundation of China under Grant 61921001, Grant 62201591, Grant 62105363, and Grant 62035014. *(Corresponding author: Bin Deng.)*

Xiaoyu Qin, Bin Deng, Hongqiang Wang, Yang Zeng, and Xu Chen are with the College of Electronic Science and Technology, National University of Defense Technology (NUDT), Changsha 410073, China (e-mail: qinxiaoyu0905@163.com; dengbin@nudt.edu.cn; wanghongqiang@nudt.edu.cn; zengyang@nudt.edu.cn; xuchen95909@126.com).

Han Xiao is with the Beijing Institute of Radio Measurement, Beijing 100854, China, and also with the Second Institute of Aerospace Science and Technology Corporation, Beijing 100854, China (e-mail: 520043801@qq.com).

Digital Object Identifier 10.1109/JSTARS.2024.3386583

other is the parametric method grounded in optimization. Motion compensation-based methods involve modeling the error factors, and estimating velocity parameters (range velocities and azimuthal velocities) or Doppler parameters (centers and slopes) of the moving target. Subsequently, the matched filter function is designed to compensate for phase errors introduced by the target's moving, facilitating the focused imaging of moving targets. In [4], [5], and [6], methods proposed to correct the range migration and estimate the motion parameter compensation to achieve the imaging of SAR ground moving targets by utilizing the second-order Keystone transform (KT), the Doppler KT, and the fractional Fourier transform (FrFT), respectively. However, these algorithms primarily address scenarios where the target is in uniform motion and do not take into account the high-frequency vibration effects of the airborne platform. Optimization-based methods [7], [8], [9], [10], on the other hand, typically involved parametric modeling of the moving target imaging model. Then, the imaging was performed by applying classical compressive sensing algorithms, such as orthogonal matching pursuit (OMP), smoothed L_0-norm, and sparse Bayesian learning, to solve the optimization inverse problem. However, it is worth highlighting that these algorithms tend to have heavy computational complexity, resulting in lower imaging efficiency.

The alternating direction method of multipliers (ADMM) is a widely employed algorithm for decomposable convex optimization problems, primarily addressing equatorially constrained optimization-like problems featuring two optimization variables. In [11], [12], and [13], the ADMM algorithm found application in sparse aperture-inverse synthetic aperture radar (ISAR) imaging to address the underdetermined sparse constraint problem, reconstructing ISAR images from sparse aperture data. The minimum entropy criterion was employed throughout the reconstruction process to estimate and compensate for phase errors in each pulse. The algorithm leads to outstanding focusing performance and high computational efficiency. Chen et al. [14], [15] employed the ADMM algorithm for near-field millimeter-wave sparse multiple-input–multiple-output SAR imaging, enabling high-quality image fast reconstruction under a large dynamic range. In another work [16], ADMM was applied to THz-SAR imaging, showcasing a notable impact on the refocusing of point targets. Nevertheless, while this method notably enhances the refocusing of point targets, it does not consider the imaging of extended targets.

Moreover, current research on SAR moving target imaging predominantly utilizes the radar in the microwave band. The traditional chirp rate compensation algorithm still primarily addresses the microwave frequency band, overlooking the high-frequency vibration of the airborne platform. In this situation, the azimuthal chirp rate remains approximately straight, allowing for direct extraction exploiting techniques, such as the Hough transform or curve fitting. However, in THz-SAR, the high-frequency vibration of the airborne platform becomes nonnegligible, and the vibration pattern is unknown, posing challenges in estimating the vibration coefficient from the data. Previous research usually assumed that the high-frequency vibration comprised fewer simple harmonic components [17], [18], [19]. Researchers commonly employed techniques including discrete sinusoidal frequency modulation transform, sinusoidal frequency modulation Fourier transform, and FrFT. These methods were combined with intelligent optimization algorithms for parameter estimation of the vibration parameters. However, as the number of simple harmonic components of the vibration increases, the accuracy of parameter estimation tends to decline. In more severe cases, this degradation in accuracy may even result in the failure of the method. Therefore, this article proposes a novel high-resolution imaging algorithm based on equalized ADMM for the reconstruction of extended ground-moving targets in THz-SAR.

The rest of this article is organized as follows. Section II establishes the echo model for THz-SAR moving targets, accounting for the high-frequency vibration from the airborne platform. Subsequently, Section III introduces an equalized ADMM-based high-resolution autofocusing imaging algorithm for ground-moving targets. The specific flow of the proposed algorithm is outlined for clarity. In Section IV, imaging experiments are conducted utilizing both simulated extended targets and measured data. The performance of the proposed algorithm is compared with existing methods to validate its effectiveness, and an analysis of imaging indices is carried out. The results obtained demonstrate the effectiveness of the method proposed in this article. Finally, Section V concludes this article.

II. Signal Model

In the microwave band, the impact of nonideal motion on the airborne platform is typically deemed negligible due to lower imaging precision. However, in the THz wave band, although imaging accuracy is enhanced, at the same time, the THz-SAR suffers from the problem of extreme sensitivity to the high-frequency vibration of the platform, necessitating a more sophisticated motion compensation algorithm. The SAR ground moving target motion model is illustrated in Fig. 1. The *X*-axis denotes the coordinate axis for the direction of motion of the airborne platform, the *Z*-axis is the coordinate axis perpendicular to the aircraft of motion of the ground target, and the *Y*-axis represents the coordinate axis perpendicular to both the *X*- and *Z*-axes, respectively.

Assuming that the airborne platform operates in the side-looking mode, we analyze the single-point imaging process to delve deeper into the target imaging characteristics. The initial position of point *P* is given by (x_0, y_0, z_0), the aircraft movement direction is azimuth direction (slow time direction), the direction of the radar transmits electromagnetic waves represents range direction (fast time direction). The height of the aircraft is *H*, the speed of motion is v_a, and the closest distance between the airborne platform and the point *P* is denoted as $R_0 = \sqrt{x_0^2 + y_0^2 + H^2}$. The target is in uniformly accelerated motion with velocity *v* and acceleration *a*, decomposed into v_x, v_y, a_x, and a_y along the *X*- and *Y*-axes, respectively.

It is assumed that the vibration of the airborne platform closely approximates the superposition of several simple harmonic motion components with different frequencies. We model the components of this periodic vibration along the radar line-of-sight

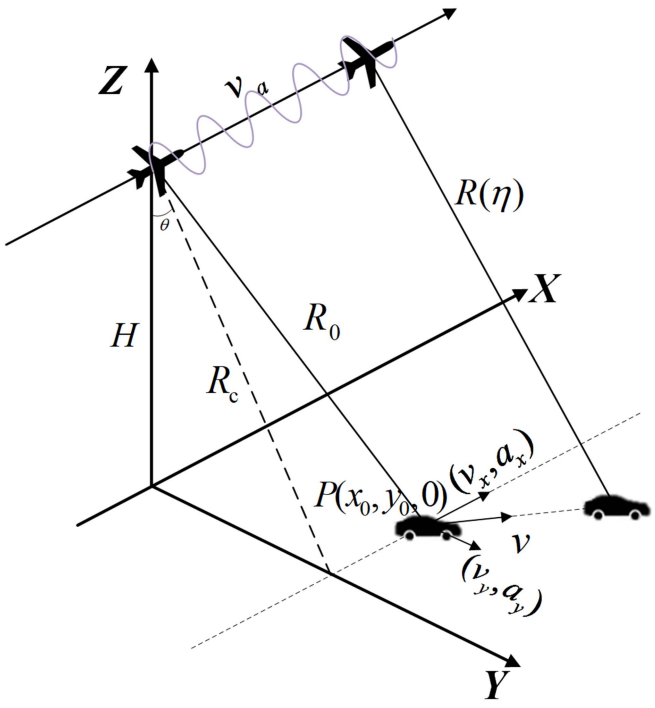

Fig. 1. SAR ground moving target motion model.

direction as $r_{\mathrm{H}}(\eta) = \sum_{i=1}^{I} A_i \sin(2\pi f_i \eta + \varphi_i)$, where η represents the slow time, I is the number of vibration components, and A_i, f_i, and φ_i denote the amplitude, frequency, and initial phase of the ith vibration component, respectively. The condition that must be satisfied for high-frequency vibration is $|f_v \cdot T_s| \geq 1$, and the synthetic aperture time of THz-SAR is about 0.2 s. Therefore, as long as the vibration frequency is over 5 Hz, it can be considered a high-frequency vibration. When high-frequency vibration exists on the radar platform, the instantaneous distance from the radar to the point P on the moving target in the scene is

$$R(\eta) = \left\{ H^2 + \left[(v_a - v_x)\eta - \frac{1}{2} a_x \eta^2 - x_0 \right]^2 + \left(y_0 + v_y \eta + \frac{1}{2} a_y \eta^2 \right)^2 \right\}^{\frac{1}{2}} + \sum_{i=1}^{I} A_i \sin(2\pi f_i \eta + \varphi_i). \quad (1)$$

The radar transmits a linear frequency modulated (LFM) signal, expressed as

$$s(\tau, \eta) = \mathrm{rect}\left(\frac{\tau}{T_{\mathrm{p}}} \right) \exp\left[\mathrm{j}2\pi \left(f_{\mathrm{c}} t + \frac{1}{2} \gamma \tau^2 \right) \right] \quad (2)$$

where rect(u) represents the rectangular envelope function, T_p denotes the signal pulse width, f_{c} is the LFM signal centre frequency, γ represents the chirp rate, $\tau = t - mT$ stands for the fast time, η is the slow time, T is the pulse repetition period, and m denotes the number of pulses.

The reference distance for Dechirp is defined as $R_{\mathrm{ref}} = \sqrt{H^2 + y_0^2}$, then the reference signal can be denoted as

$$s_{\mathrm{ref}}(\tau, \eta) = \mathrm{rect}\left(\frac{\tau - 2R_{\mathrm{ref}}}{T_{\mathrm{ref}}} \right) \times \exp\left\{ \mathrm{j}2\pi \left[f_{\mathrm{c}} \left(t - \frac{2R_{\mathrm{ref}}}{c} \right) + \frac{1}{2} \gamma \left(\tau - \frac{R_{\mathrm{ref}}}{c} \right)^2 \right] \right\}. \quad (3)$$

The echo signal received by the radar is represented as

$$s_{\mathrm{r}}(\tau, \eta) = A\mathrm{rect}\left(\frac{\tau - 2R(\eta)}{T_{\mathrm{p}}} \right) \times \exp\left\{ \mathrm{j}2\pi \left[f_{\mathrm{c}} \left(t - \frac{2R(\eta)}{c} \right) + \frac{1}{2} \gamma \left(\tau - \frac{R(\eta)}{c} \right)^2 \right] \right\}. \quad (4)$$

Let $R_\Delta = R(\eta) - R_{\mathrm{ref}}$. The resulting differential frequency signal output is

$$s(\tau, \eta) = A\mathrm{rect}\left(\frac{\tau - 2R_\Delta / c}{T_{\mathrm{p}}} \right) \cdot \exp\left(\mathrm{j} \frac{4\pi\gamma}{c^2} R_\Delta^2 \right) \times \exp\left(-\mathrm{j} \frac{4\pi}{c} f_{\mathrm{c}} R_\Delta \right) \cdot \exp\left[-\mathrm{j} \frac{4\pi}{c} \gamma \left(\tau - \frac{2R_{\mathrm{ref}}}{c} \right) R_\Delta \right]. \quad (5)$$

After correcting for the residual video phase (RVP), the range compressed signal can be obtained as

$$s(f_i, \eta) = \mathrm{FT}(s(\tau, \eta)) \cdot \exp\left(-\mathrm{j}\,\pi {f_i}^2 / \gamma \right) = A T_{\mathrm{p}} \mathrm{sinc}\left[T_{\mathrm{p}} \left(f_i + \frac{2\gamma R_\Delta}{c} \right) \right] \cdot \exp\left(-\mathrm{j}4\pi f_{\mathrm{c}} R_\Delta / c \right). \quad (6)$$

III. Equalized ADMM-Based THz-SAR Ground Moving Target Imaging Algorithm

According to the theory of compressive sensing, the range compression echo signal (6) is expressed as a matrix form, denoted as $\mathbf{S} \in \mathbb{C}^{N \times M}$, where $\mathbf{S}$ represents the range profile, N is the number of azimuthal sampling points, and M denotes the number of range sampling points. In the ISAR turntable imaging model, the ISAR image can be obtained by directly applying the inverse fast Fourier transform (IFFT) to the range profile. However, for SAR imaging, it is necessary to multiply the signal $\mathbf{S}$ by the compensation matrix in azimuth direction $\mathbf{E}_1$ and then carry out IFFT in the azimuth to obtain the focused SAR image. At this point, the sequence of range profiles can be expressed as

$$\mathbf{S} = \mathbf{E}_1 \mathbf{F} \mathbf{X} \quad (7)$$

where $\mathbf{F}$ is the Fourier matrix and the element values in the matrix are $\mathbf{F}_{i,j} = \frac{1}{\sqrt{N}} \exp[-\mathrm{j}\frac{2\pi}{N}(i-1)(j-1)]$, $\mathbf{E}_1 = \mathrm{diag}[\exp(\mathrm{j}\boldsymbol{\varphi})]$ is the azimuthal phase error matrix, diag($\cdot$) denotes the diagonal matrix formed with vectors, and $\boldsymbol{\varphi} \in \mathbb{R}^N$ represents the phase error at each pulse.

For the SAR image, both the target and the background are present. To better extract the moving target, it is essential to

separate it from the background. By considering the low-rank and sparse characteristics of the moving target in the SAR image, the moving target imaging model is constructed

$$\begin{aligned} &\min \operatorname{rank}(\mathbf{T}) + \alpha_1 ||\mathbf{G}||_0 + \alpha_2 ||\mathbf{X}||_0 \\ &\text{s.t.}\ \mathbf{S} = \mathbf{T} + \mathbf{G} \\ &\quad \mathbf{T} = \mathbf{EFX} \end{aligned} \tag{8}$$

where α_1 and α_2 are regularization parameters, the range profile $\mathbf{S}$ is divided into the range profile $\mathbf{T} \in \mathbb{C}^{N\times M}$ of the target and the range profile $\mathbf{G} \in \mathbb{C}^{N\times M}$ of the background noise, and $\mathbf{E} \in \mathbb{C}^{N\times N}$ denotes the azimuthal phase error matrix. Since the l_0 norm constraint leads to an N-P hard problem for which an exact solution cannot be found, the l_1 norm is commonly utilized to replace the l_0 norm, making the above optimization problem a solvable convex optimization problem. Furthermore, the nuclear norm is typically utilized to represent the low-rank constraint, so the (8) can be represented as

$$\begin{aligned} &\min \operatorname{rank}(\mathbf{T}) + \alpha_1 ||\mathbf{G}||_1 + \alpha_2 ||\mathbf{X}||_1 \\ &\text{s.t.}\ \ \mathbf{S} = \mathbf{T} + \mathbf{G} \\ &\quad \mathbf{T} = \mathbf{EFX}. \end{aligned} \tag{9}$$

It can be seen that (9) is a triply-constrained convex optimization problem. The ADMM algorithm provides a framework for solving optimization problems containing linear equation constraints, which facilitates us to disassemble the original multiconstraint optimization problem into several relatively solvable suboptimization problems for iterative solving. However, noting that the coefficient of $\mathbf{X}$ in the objective function is not identity and cannot be utilized in the ADMM framework directly. We adopt the form of introducing an auxiliary variable $\mathbf{Z}$ to solve this problem

$$\begin{aligned} &\min ||\mathbf{T}||_* + \alpha_1 ||\mathbf{G}||_1 + \alpha_2 ||\mathbf{Z}||_1 \\ &\text{s.t.}\ \ \mathbf{S} = \mathbf{T} + \mathbf{G} \\ &\quad \mathbf{T} = \mathbf{EFX} \\ &\quad \mathbf{X} = \mathbf{Z}. \end{aligned} \tag{10}$$

In the high-frequency domain, the representation of the target scattering characteristics can be described by the structure of the distribution of numerous scattering centers, displaying cluster sparsity in SAR images. This means that the scatterers are not isolated. To enhance the quality of SAR imaging, we introduce the continuity of the scatterers into the l_1 minimization, rather than the simplistic application of the least absolute shrinkage and selection operator model. We employ a 5×5 convolutional kernel on the image obtained through the previous iteration for equalization smoothing by reweighting the conventional l_1 norm, thus enhancing the continuity of the image, as illustrated in Fig. 2.

We design the weighting function in the form of $1/\lg(\beta \cdot \mathcal{C}\mathbf{X} + 1)$, where $\mathcal{C}$ is the convolution operator. As the target image encompasses a wide dynamic range, employing a logarithmic threshold function contributes to preserving the fine structure of the SAR image to the fullest extent possible, preventing over-penalization while smoothing the image. The adjustable parameter β is introduced to accommodate different scenario requirements. At this point, the optimization problem presented in (10) can be further rewritten as

0.5	0.5	0.5	0.5	0.5
0.5	1	1	1	0.5
0.5	1	1	1	0.5
0.5	1	1	1	0.5
0.5	0.5	0.5	0.5	0.5

Fig. 2. Equalized smoothing convolution kernel.

$$\begin{aligned} &\min ||\mathbf{T}||_* + \alpha_1 ||\mathbf{G}||_1 + \alpha_2 \left|\left| \frac{1}{\lg(\beta \cdot \mathcal{C}\mathbf{X}^{(k)} + 1)} \odot \mathbf{Z} \right|\right|_1 \\ &\text{s.t.}\ \mathbf{S} = \mathbf{T} + \mathbf{G} \\ &\quad \mathbf{T} = \mathbf{EFX} \\ &\quad \mathbf{X} = \mathbf{Z} \end{aligned} \tag{11}$$

where the symbol $\odot$ denotes the element-by-element multiplication of the matrix.

Given the above analysis, the augmented Lagrangian function can be denoted as follows:

$$\begin{aligned} &\mathcal{L}(\mathbf{T}, \mathbf{G}, \mathbf{X}, \mathbf{Z}, \mathbf{u}_1, \mathbf{u}_2, \mathbf{u}_3) \\ &= ||\mathbf{T}||_* + \alpha_1 ||\mathbf{G}||_1 + \alpha_2 \left|\left| \frac{1}{\lg(\beta \cdot \mathcal{C}\mathbf{X}^{(k)} + 1)} \odot \mathbf{Z} \right|\right|_1 \\ &\quad + \mathbf{u}_1^{\mathrm{H}}(\mathbf{S} - \mathbf{T} - \mathbf{G}) + \mathbf{u}_2^{\mathrm{H}}(\mathbf{T} - \mathbf{EFX}) + \mathbf{u}_3^{\mathrm{H}}(\mathbf{X} - \mathbf{Z}) \\ &\quad + \frac{\rho_1}{2} ||\mathbf{S} - \mathbf{T} - \mathbf{G}||_F^2 + \frac{\rho_2}{2} ||\mathbf{T} - \mathbf{EFX}||_F^2 + \frac{\rho_3}{2} ||\mathbf{X} - \mathbf{Z}||_F^2 \end{aligned} \tag{12}$$

where $\mathbf{u}_1$, $\mathbf{u}_2$, and $\mathbf{u}_3$ denote the Lagrange multiplier matrices and ρ_1, ρ_2, and ρ_3 are the penalty parameters. Then, ADMM solves the optimization problem in (11) by decomposing it into

the following more tractable subproblems:

$$\begin{cases} \mathbf{T}^{(k+1)} = \min\limits_{\mathbf{T}} \mathcal{L}\left(\mathbf{T}, \mathbf{G}^{(k)}, \mathbf{X}^{(k)}, \mathbf{Z}^{(k)}, \mathbf{u}_1^{(k)}, \mathbf{u}_2^{(k)}, \mathbf{u}_3^{(k)}\right) \\ \mathbf{G}^{(k+1)} = \min\limits_{\mathbf{N}} \mathcal{L}\left(\mathbf{T}^{(k+1)}, \mathbf{G}, \mathbf{X}^{(k)}, \mathbf{Z}^{(k)}, \mathbf{u}_1^{(k)}, \mathbf{u}_2^{(k)}, \mathbf{u}_3^{(k)}\right) \\ \mathbf{X}^{(k+1)} = \min\limits_{\mathbf{X}} \mathcal{L}\left(\mathbf{T}^{(k+1)}, \mathbf{G}^{(k+1)}, \mathbf{X}, \mathbf{Z}^{(k)}, \mathbf{u}_1^{(k)}, \mathbf{u}_2^{(k)}, \mathbf{u}_3^{(k)}\right) \\ \mathbf{Z}^{(k+1)} = \min\limits_{\mathbf{Z}} \mathcal{L}\left(\mathbf{T}^{(k+1)}, \mathbf{G}^{(k+1)}, \mathbf{X}^{(k+1)}, \right. \\ \qquad \left. \mathbf{Z}, \mathbf{u}_1^{(k)}, \mathbf{u}_2^{(k)}, \mathbf{u}_3^{(k)}\right) \\ \mathbf{u}_1^{(k+1)} = \mathbf{u}_1^{(k)} + \rho_1^{(k)}\left(\mathbf{S} - \mathbf{T}^{(k+1)} - \mathbf{G}^{(k+1)}\right) \\ \mathbf{u}_2^{(k+1)} = \mathbf{u}_2^{(k)} + \rho_2^{(k)}\left(\mathbf{T}^{(k+1)} - \mathbf{E}\mathbf{F}\mathbf{X}^{(k+1)}\right) \\ \mathbf{u}_3^{(k+1)} = \mathbf{u}_3^{(k)} + \rho_3^{(k)}\left(\mathbf{X}^{(k+1)} - \mathbf{Z}^{(k+1)}\right) \\ {\rho_{1,2,3}}^{(k+1)} = {\rho_{1,2,3}}^{(k)}. \end{cases} \tag{13}$$

Address the subproblems in (13) sequentially. First, we update the range profile of the target, which is a nuclear norm convex problem that can be solved analytically by the singular value thresholding algorithm [20], [21].

Let

$$\mathbf{H}^{(k)} = \frac{\rho_1^{(k)}}{\rho_1^{(k)} + \rho_2^{(k)}}\left(\mathbf{S} - \mathbf{G}^{(k)}\right) + \frac{\rho_2^{(k)}}{\rho_1^{(k)} + \rho_2^{(k)}}\mathbf{E}\mathbf{F}\mathbf{X}^{(k)} + \frac{1}{\rho_1^{(k)} + \rho_2^{(k)}}\left(\mathbf{u}_1^{(k)} - \mathbf{u}_2^{(k)}\right) \tag{14}$$

then we have

$$\mathbf{T}^{(k+1)} = \mathbf{U}^{(k)} \cdot \mathcal{S}_{\frac{1}{\rho_1^{(k)} + \rho_2^{(k)}}}\left(\mathbf{\Sigma}^{(k)}\right) \cdot \left(\mathbf{V}^{(k)}\right)^{\mathrm{H}} \tag{15}$$

where $\mathbf{H}^{(k)} = \mathbf{U}^{(k)} \cdot \mathbf{\Sigma}^{(k)} \cdot \left(\mathbf{V}^{(k)}\right)^{\mathrm{H}}$, $\mathbf{U}^{(k)}$ and $\mathbf{V}^{(k)}$ are matrices consisting of the left and right singular vectors of $\mathbf{H}^{(k)}$, respectively, and $\mathbf{\Sigma}^{(k)}$ is a diagonal matrix consisting of the singular values. $\mathcal{S}_\gamma(x)$ denotes the soft thresholding operator for an arbitrary variable x as $\mathcal{S}_\gamma(x) = \mathrm{sgn}(x)(|x| - \gamma)_+$.

Proceed to update the background noise matrix $\mathbf{G}$, constituting a standard l_1 norm minimization problem, the analytical solution of which can be obtained by the soft threshold operator

$$\mathbf{G}^{(k+1)} = \mathcal{S}_{\frac{\alpha_1}{\rho_1^{(k)}}}\left(\mathbf{S} - \mathbf{T}^{(k+1)} + \frac{1}{\rho_1^{(k)}}\mathbf{u}_1^{(k)}\right). \tag{16}$$

Then, the image of the target's main body part can be updated by the following equation:

$$\mathbf{X}^{(k+1)} = \left(\rho_2^{(k)}\mathbf{I} + \rho_3^{(k)}\mathbf{I}\right)^{-1}\left[\mathbf{F}^{\mathrm{H}}\left(\mathbf{E}^{\mathrm{H}}(\mathbf{u}_2^{(k)} + \rho_2^{(k)}\mathbf{T}^{(k+1)}) + \rho_3^{(k)}\mathbf{F}\mathbf{Z}^{(k)} - \mathbf{F}\mathbf{u}_3^{(k)}\right)\right] \tag{17}$$

where the matrix $\mathbf{F}$ and matrix $\mathbf{F}^{\mathrm{H}}$ can be computed quickly by and IFFT, respectively, to improve the computational efficiency.

The subsequent step is to update the auxiliary variable $\mathbf{Z}$, which is similar to (16) and can be derived utilizing the soft threshold operator

$$\mathbf{Z}^{(k+1)} = \mathcal{S}_{\frac{\alpha_2}{\rho_3^{(k)}\lg(\beta\cdot|\mathbf{C}\mathbf{X}^{(k+1)}|+1)}}\left(\mathbf{X}^{(k+1)} + \frac{1}{\rho_3^{(k)}}\mathbf{u}_3^{(k)}\right). \tag{18}$$

In fact, just updating (13) does not yield the target image. We must simultaneously compensate for the azimuthal error matrix $\mathbf{E}$ to obtain the high-quality image by iteration. Image entropy serves as an evaluation criterion for the quality of image focusing, reflecting the degree of system confusion. A lower image entropy indicates better image focusing. The azimuthal error matrix $\mathbf{E}$ can be solved by minimizing the image entropy [22], [22]. The image entropy corresponding to the target image $\mathbf{X}^{(k)}$ obtained in the kth iteration can be expressed as

$$E_{\mathbf{X}^{(k)}} = \ln S_{\mathbf{X}^{(k)}} - \frac{1}{S_{\mathbf{X}^{(k)}}}\sum_{n=1}^{N}\sum_{m=1}^{M}\left[|\mathbf{X}^{(k)}(n,m)|^2 \times \ln\left(|\mathbf{X}^{(k)}(n,m)|^2\right)\right] \tag{19}$$

where $S_{\mathbf{X}^{(k)}}$ denotes the energy of the image

$$S_{\mathbf{X}^{(k)}} = \sum_{n=1}^{N}\sum_{m=1}^{M}|\mathbf{X}^{(k)}(n,m)|^2. \tag{20}$$

The phase error can be estimated by utilizing the minimum entropy criterion. Therefore, we calculate the derivative of the image entropy concerning the phase error φ_i corresponding to the ith pulse

$$\frac{\partial E_{\mathbf{X}^{(k)}}}{\partial \varphi_i} = -\frac{2}{S_{\mathbf{X}^{(k)}}}\sum_{n=1}^{N}\sum_{m=1}^{M}\left[1 + \ln\ |\mathbf{X}^{(k)}(n,m)|^2\right] \times \mathrm{Re}\left(\mathbf{X}^{(k)*}(n,m) \cdot \frac{\partial \mathbf{X}^{(k)}(n,m)}{\partial \varphi_i}\right). \tag{21}$$

Let the derivative be equal to zero, the estimate of each azimuthal error φ_i can be denoted as

$$\varphi_i^{(k)} = \mathrm{phase}\left\{\sum_{n=1}^{N}\sum_{m=1}^{M}\left[\left(1 + \ln|\mathbf{X}^{(k)}(n,m)|^2\right) \times \mathbf{X}^{(k)*}(n,m) \cdot \mathbf{F}^{\mathrm{H}} \cdot \mathbf{T'}_i\right]\right\}, i = 1, 2, \ldots, N \tag{22}$$

where

$$\mathbf{T'}_i = \begin{bmatrix} \mathbf{0}_{(i-1)\times M} \\ \mathbf{T}_i \\ \mathbf{0}_{(N-i)\times M} \end{bmatrix} \tag{23}$$

and $\mathbf{T}_i$ represents the moving target's range profile corresponding to the ith pulse. The phase$(\cdot)$ denotes taking the phase operator.

Therefore, we obtain the updated expression for the azimuthal error matrix $\mathbf{E}$ as

$$\mathbf{E}^{(k+1)} = \mathrm{diag}\left[\exp\left(\mathrm{j}\varphi_1^{(k)}\right), \exp\left(\mathrm{j}\varphi_2^{(k)}\right), \ldots, \exp\left(\mathrm{j}\varphi_N^{(k)}\right)\right]. \tag{24}$$

Finally, we can obtain the following SAR moving target imaging procedure based on ADMM with autofocus as indicated

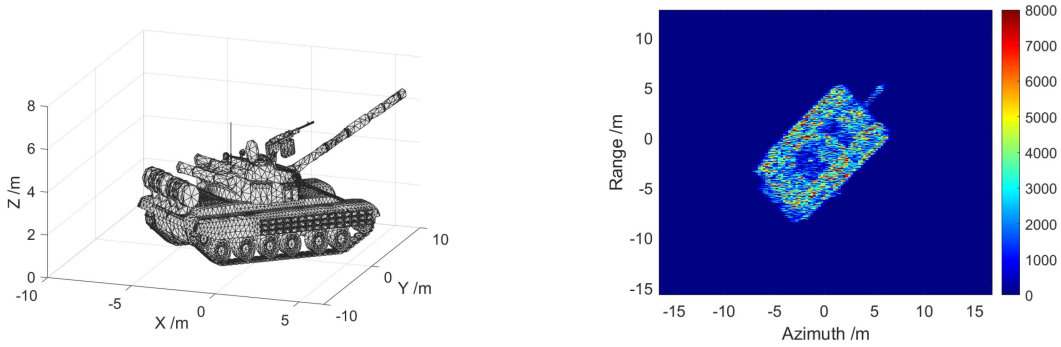

(a) (b)

Fig. 3. Target point cloud map and the imaging results of the ideal stationary situation. (a) Target point cloud map. (b) Imaging results of RDA in the stationary situation.

TABLE I
THE MAIN PARAMETERS OF THE RADAR SYSTEM

Parameter	Value
Flight velocity of SAR platform	60 m/s
Height of SAR platform	1300 m
Carrier frequency	220 GHz
Bandwidth	1 GHz
Pulse repetition frequency	16000 Hz
Length of synthetic aperture	7.2 m

in the following:

$$\begin{cases} \mathbf{H}^{(k)} = \frac{\rho_1^{(k)}}{\rho_1^{(k)}+\rho_2^{(k)}}(\mathbf{S}-\mathbf{G}^{(k)}) + \frac{\rho_2^{(k)}}{\rho_1^{(k)}+\rho_2^{(k)}}\mathbf{E}^{(k)}\mathbf{F}\mathbf{X}^{(k)} \\ \quad + \frac{1}{\rho_1^{(k)}+\rho_2^{(k)}}\left(\mathbf{u}_1^{(k)}-\mathbf{u}_2^{(k)}\right) \\ \mathbf{T}^{(k+1)} = \mathbf{U}^{(k)} \cdot \mathcal{S}_{\frac{1}{\rho_1^{(k)}+\rho_2^{(k)}}}\left(\mathbf{\Sigma}^{(k)}\right) \cdot \left(\mathbf{V}^{(k)}\right)^H \\ \mathbf{G}^{(k+1)} = \mathcal{S}_{\frac{\alpha_1}{\rho_1^{(k)}}}\left(\mathbf{S}-\mathbf{T}^{(k+1)}+\frac{1}{\rho_1^{(k)}}\mathbf{u}_1^{(k)}\right) \\ \mathbf{X}^{(k+1)} = \left(\rho_2^{(k)}\mathbf{I}+\rho_3^{(k)}\mathbf{I}\right)^{-1}\left[\mathbf{F}^{\mathrm{H}}\left(\mathbf{E}^{\mathrm{H}}(\mathbf{u}_2^{(k)}\right.\right. \\ \quad \left.\left.+\rho_2^{(k)}\mathbf{T}^{(k+1)}\right)+\rho_3^{(k)}\mathbf{F}\mathbf{Z}^{(k)}-\mathbf{F}\mathbf{u}_3^{(k)}\right)\right] \\ \mathbf{Z}^{(k+1)} = \mathcal{S}_{\frac{\alpha_2}{\rho_3^{(k)}\lg(\beta\cdot|\mathcal{C}\mathbf{X}^{(k+1)}|+1)}}\left(\mathbf{X}^{(k+1)}+\frac{1}{\rho_3^{(k)}}\mathbf{u}_3^{(k)}\right) \\ \mathbf{E}^{(k+1)} = \mathrm{diag}\left[\exp\left(\mathrm{j}\varphi_1^{(k)}\right),\exp\left(\mathrm{j}\varphi_2^{(k)}\right),\ldots,\exp\left(\mathrm{j}\varphi_N^{(k)}\right)\right] \\ \mathbf{u}_1^{(k+1)} = \mathbf{u}_1^{(k)}+\rho_1^{(k)}\left(\mathbf{S}-\mathbf{T}^{(k+1)}-\mathbf{G}^{(k+1)}\right) \\ \mathbf{u}_2^{(k+1)} = \mathbf{u}_2^{(k)}+\rho_2^{(k)}\left(\mathbf{T}^{(k+1)}-\mathbf{E}\mathbf{F}\mathbf{X}^{(k+1)}\right) \\ \mathbf{u}_3^{(k+1)} = \mathbf{u}_3^{(k)}+\rho_3^{(k)}\left(\mathbf{X}^{(k+1)}-\mathbf{Z}^{(k+1)}\right) \\ {\rho_{1,2,3}}^{(k+1)} = {\rho_{1,2,3}}^{(k)}. \end{cases} \tag{25}$$

IV. NUMERICAL SIMULATION AND EXPERIMENTAL VERIFICATION

A. Numerical Simulation

We construct the point cloud target to simulate the extended target utilizing simulation software, as illustrated in Fig. 3(a). The simulation parameters for the radar are set in Table I. To align simulation results with reality, the angle between radar incidence and the point cloud surface element is utilized as the criterion to determine whether the element is in the shadow of the radar. The imaging result under the ideal situation when the target is stationary as displayed in Fig. 3(b). According to (5), the primary determinant influencing Doppler central phase variation is the range velocity of the target, leading to an azimuthal position offset for the moving target. In addition, azimuthal velocity and range acceleration are vital contributors to the change in Doppler chirp rate, causing the target to defocus in the azimuth direction. In this article, we focus on the azimuth-defocusing issue of the target, so the range velocity and azimuthal acceleration are set to be zero in the simulation for simplicity. The azimuthal velocity and the range acceleration of the target are chosen to be 10 m/s and 2 m/s^2 in our simulations. Furthermore, we have modeled the high-frequency vibration of the airborne platform utilizing three simple harmonic components superimposed, as depicted in the following:

$$\begin{aligned} r_{\mathrm{H}}(\eta) = {} & 0.001\sin(90\pi\eta+\pi/4)+0.0012\sin(60\pi\eta+\pi/6) \\ & +0.0018\sin(40\pi\eta+\pi/3). \end{aligned} \tag{26}$$

The range profile of the target and the outcome of time–frequency analysis utilizing short-time Fourier transform (STFT) are presented in Fig. 4. At this time, due to the high-frequency vibration of the airborne platform, the Doppler frequency of the echo signal is no longer a straight line. Consequently, compensating for the Doppler chirp rate through the conventional method based on estimating velocity parameters becomes unfeasible.

The outcome of coarse imaging utilizing the range-Doppler algorithm (RDA) for the point cloud target is displayed in Fig. 5(a). The impact of high-frequency vibration of the airborne platform in the THz wave band can not be overlooked, resulting in serious defocusing of the target imaging results, and even the shape of the target can hardly be recognized.

Fig. 5(b) depicts the imaging results after 2000 iterations applying the conventional phase gradient autofocus (PGA) algorithm. Despite a slight improvement in focus compared with the coarse imaging results obtained with RDA, the target remains unrecognizable.

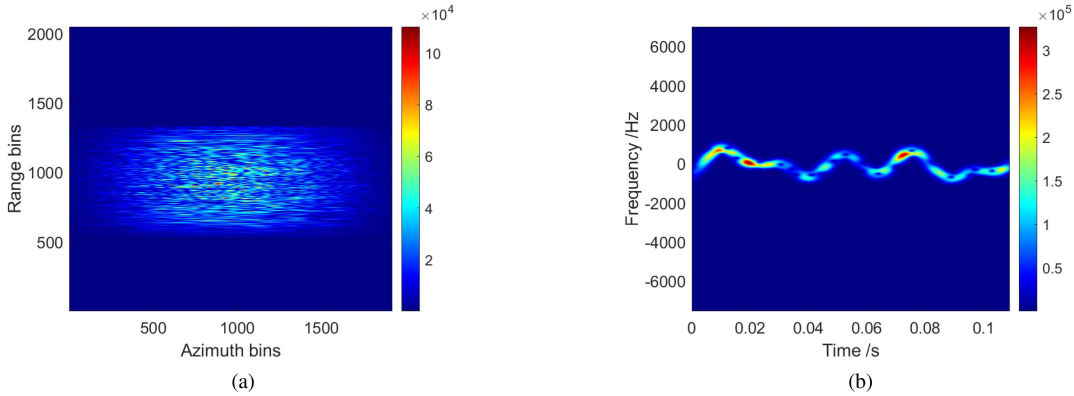

Fig. 4. Range profile of the simulated moving target and the result of the time-frequency analysis. (a) Range profile of the target. (b) Time–frequency analysis result.

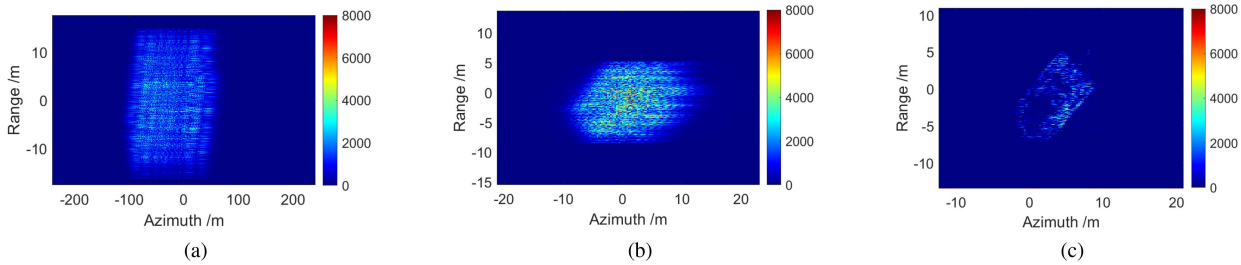

Fig. 5. Imaging results. (a) RDA imaging result. (b) PGA imaging result. (c) Imaging result of the proposed algorithm.

TABLE II
NUMERICAL RESULTS OF SIMULATED DATA UNDER DIFFERENT IMAGING ALGORITHMS

Algorithm	PSLR (dB)	ISLR (dB)	SSIM	IE	IC
RDA	-4.0665	-1.7797	0.2933	11.3144	2.9925
PGA	-8.1934	0.3021	0.8936	10.2680	5.3082
Proposed	**-12.8392**	**-12.5796**	**0.9396**	**7.9610**	**19.1807**

Fig. 5(c) demonstrates the imaging results employing the equalized ADMM autofocusing algorithm proposed in this article. The penalty parameters, ρ_1, ρ_2, and ρ_3 are set to be equivalent, which are suggested to be relevant to the reciprocal of the Frobenius norm of the range profile sequence [21]. In our experiments, they are set as $\rho_1 = \rho_2 = \rho_3 = 1$. In addition, in this article, β is set to 1.2 to accelerate convergence after the smooth equalization operation, which can be adjusted by using grid search method. The parameters of the subsequent measured experiments are set in the same way. This approach allows for complete target recovery, even capturing critical components with weak scattering, such as the gun barrel, with sufficient focus.

For a more precise assessment of imaging quality, we consider metrics, such as peak sidelobe ratio (PSLR), integrated SLR (ISLR), structural similarity (SSIM), image entropy (IE), and image contrast (IC). The comparative results are displayed in Table II, providing evidence for the effectiveness of the approach proposed in this article.

B. Experimental Verification

In this section, we utilize the measurement data to verify the proposed algorithm. The experiment was conducted at an intersection applying the spotlight SAR. Fig. 6(a) illustrates the experimental scenario, encompassing fields, villages, and roads. The red dot in the figure represents the center of the beam coverage area, and the target moves uniformly accelerated in a straight line in the direction indicated by the yellow arrow. The stationary corner reflector is positioned at the intersection for calibration purposes. One side of the road features drying corn, while the other side is paved with asphalt. The radar parameters are configured identically to the simulation scene, as depicted in Table I. We select two frames of the data for imaging processing and performance analysis and the imaging results of the scenario are demonstrated in Fig. 6(b) and (c).

To avoid the coupling effect caused by the target motion and the high-frequency vibration of the airborne platform, we verify the proposed high-frequency vibration model by utilizing the stationary corner reflector in the scenario. The range bins where the corner reflector is located in the coarse image of frames A and B are extracted, respectively, to obtain the phase curve. Therefore, the airborne platform vibration curve is recovered utilizing the relationship between phase and distance. As depicted in Fig. 7, the variation of the airborne platform is in the form of superposition of multiple sinusoidal components. The spectrum analysis is carried out, respectively, in which the lowest frequency components are greater than 10 Hz, which

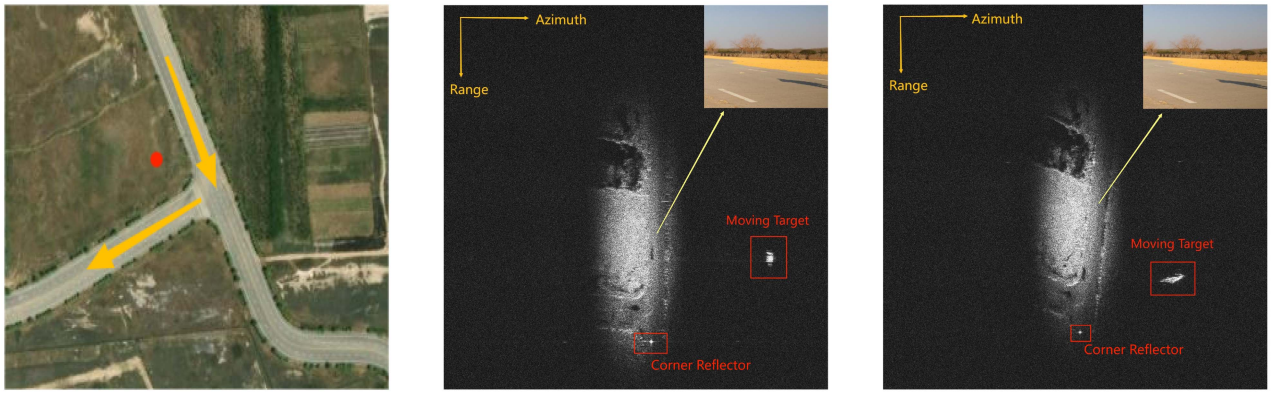

(a) (b) (c)

Fig. 6. Scenario of the field experiment. (a) Trajectory map of the target. (b) Optical scenario and coarse imaging of frame A. (c) Optical scenario and coarse imaging of frame B.

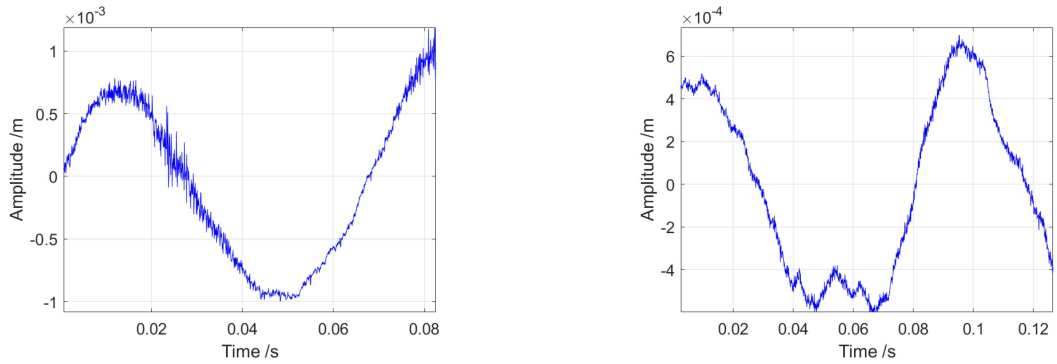

(a) (b)

Fig. 7. Airborne platform vibration curve. (a) Airborne platform vibration curve of frame A. (b) Airborne platform vibration curve of frame B.

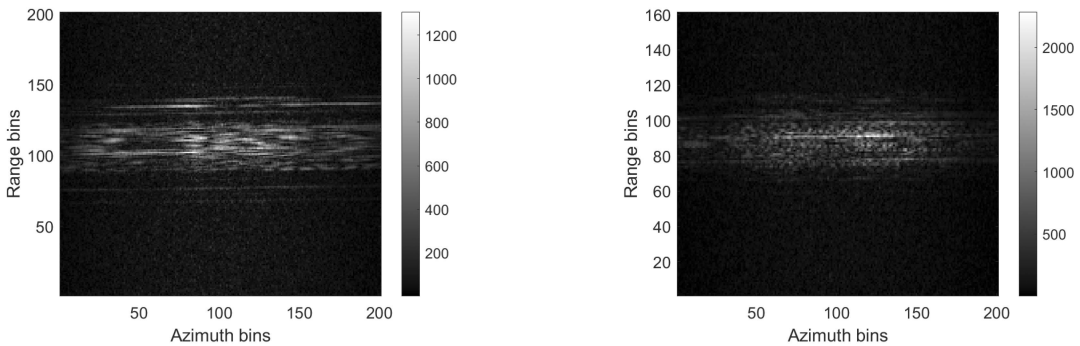

(a) (b)

Fig. 8. Moving target ROI area range profile. (a) Range profile of frame A. (b) Range profile of frame B.

satisfies the condition of $|f_v \cdot T_s| \geq 1$, and it can be considered that the vibration of the carrier is a high-frequency vibration with multiple sinusoidal components superimposed.

Based on the coarse imaging of the scenario, we select the range bins containing the moving target as the region of interest (ROI). Then, the range profile can be obtained by applying IFFT, as illustrated in Fig. 8.

The imaging results of employing RDA, STFT time-frequency analysis with PGA compensation algorithm, and the proposed algorithm, respectively, are illustrated in Fig. 9. Fig. 9(a) and (f) presents the results of coarse imaging by utilizing the RD algorithm for frame A and frame B. Initially, we perform range compression and RVP compensation of the echo data recorded by the radar. Then, we estimate the Doppler

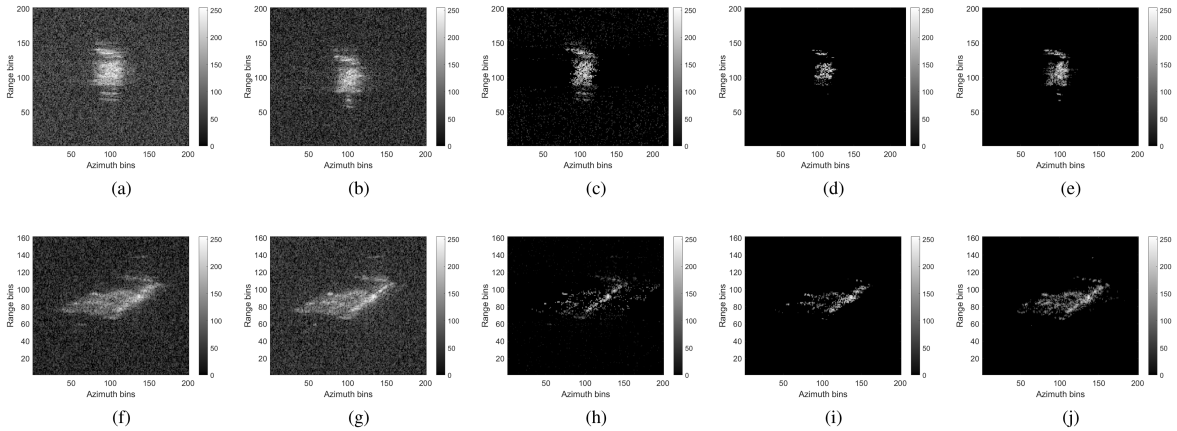

Fig. 9. Imaging results. (a) Direct RDA imaging of frame A. (b) Conventional compensated imaging of frame A. (c) OMP algorithm imaging of frame A. (d) ADMM algorithm imaging of frame A. (e) Proposed algorithm imaging of frame A. (f) Direct RDA imaging of frame B. (g) Conventional compensated imaging of frame B. (h) OMP algorithm imaging of frame B. (i) ADMM algorithm imaging of frame B. (j) Proposed algorithm imaging of frame B.

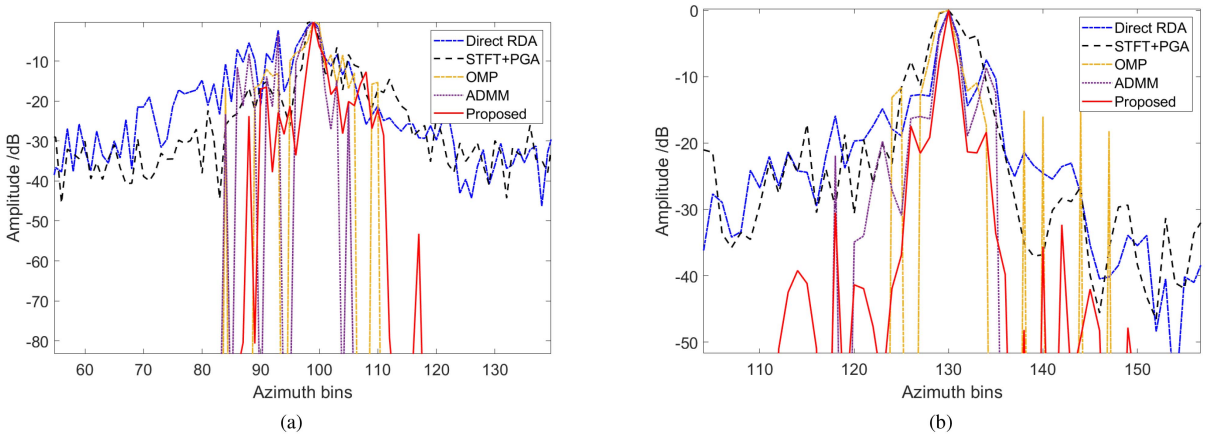

Fig. 10. Azimuth responses of the moving target. (a) Azimuth response of frame A. (b) Azimuth response of frame B.

center frequency of the scene echoes, conduct the range migration correction, and employ the airborne platform velocity to compensate for the azimuthal chirp rate coarsely. The resulting coarse imaging outcomes are depicted in the respective figures.

Fig. 9(b) and (g) illustrates the results of imaging by utilizing the classical algorithm. First, We perform the time–frequency analysis by STFT for the range profile within ROI. Subsequently, we fit the time–frequency curve to obtain the chirp rate, allowing us to construct a corresponding matched filter for azimuthal compensation. After that, the conventional PGA algorithm is utilized for 100 iterations to enhance autofocusing further. Although the compensated images of the moving target show improvement compared with the RDA's imaging results, a certain degree of defocusing is still observed, as this compensation addresses only the major effects introduced by azimuthal velocity.

Fig. 9(c) and (h) demonstrates the imaging results of the compressive sensing methods OMP. Although the OMP algorithm can recover the shape of the target, the reconstruction results have presented some false scattering points. The reason for the false scattering points is that the sparsity of the extended target cannot be determined, together with the background noise that leads to the mismatch of the sparse dictionary.

Fig. 9(d) and (i) illustrates the imaging results of a traditional ADMM, which exploits the l_1 norm to enable the imaging to be as sparse as possible. Nevertheless, as can be noticed from the figure, the gun barrel structure is not recognizable in both frames of data.

The imaging results obtained with the proposed algorithm are displayed in Fig. 9(e) and (j). Within the same dynamic range, the target and background are completely separated, while the focusing performance is enhanced. The computational platform is Intel(R) Core(TM) i9-13900HX CPU at 5.4 GHz. With 100 iterations, the proposed algorithm demonstrates a swift autofocusing capability, completing the process in only 9.523 and 8.145 s for the two scenes, respectively. The inclusion of the equalization constraint term ensures the preservation of finer details in the image, resulting in more distinct and focused representations of key components, such as the tank's gun barrel.

The azimuthal responses of the three algorithms in frames A and B are illustrated in Fig. 10, revealing that the proposed algorithm exhibits a narrower mainlobe width, lower sidelobe

TABLE III
NUMERICAL RESULTS OF MEASURED DATA UNDER DIFFERENT IMAGING ALGORITHMS

Algorithm	PSLR (dB)	ISLR (dB)	IE	IC
RDA-A	-8.4305	-5.5509	7.8414	7.1249
STFT+PGA-A	-6.5725	-2.9388	7.5752	9.2397
OMP-A	-7.9649	-4.8325	6.5904	11.7091
ADMM-A	-14.7897	-6.0820	5.3517	17.7668
Proposed-A	**-16.4894**	**-17.2947**	**5.3158**	**19.6610**
RDA-B	-7.4523	-13.9519	7.3073	12.4129
STFT+PGA-B	-3.8233	-13.2473	7.1714	11.6546
OMP-B	-10.9240	-14.1528	5.8598	19.5620
ADMM-B	-8.6592	-20.6713	4.3016	36.3047
Proposed-B	**-18.3406**	**-28.3090**	**5.0198**	**32.2654**

level, and significantly better focus compared with classical algorithms.

Similarly, we calculate the PSLR, ISLR of the strongest point target in the image, IE, and IC for a more precise evaluation of imaging quality. Since there is no ground truth imaging result for a stationary tank in the real scene, SSIM is not included in the comparison. The comparison results are displayed in Table III. Although the IE and IC of the imaging results of the proposed algorithm on data frame B are slightly inferior to those of the traditional ADMM algorithm, the PSLR index indicates that the original ADMM has no focusing capability and the weakly scattering barrel structure is penalized. However, the proposed algorithm can achieve the focusing capability while retaining the target's structure as much as possible, demonstrating the proposed approach's effectiveness.

V. CONCLUSION

In this article, a novel high-resolution imaging approach for THz-SAR ground-moving targets with equalized ADMM is proposed. The method capitalizes on the low-rank and sparse characteristics of moving targets in the SAR image to effectively distinguish the moving targets from the background. It employs the minimized image entropy for iterative to update the azimuthal matched filter during the imaging process to achieve autofocusing. In addition, it incorporates the equalization coefficient to achieve a sparse image representation while preserving target details. Compared with conventional imaging algorithms, the proposed approach substantially enhances the focusing accuracy without estimating the Doppler parameter and improves overall imaging efficiency. These advancements contribute to the subsequent implementation of tracking, classification, and intent inversion for moving targets.

REFERENCES

[1] C. A. Wiley, "Synthetic aperture radars," *IEEE Trans. Aerosp. Electron. Syst.*, vol. AES-21, no. 3, pp. 440–443, May 1985.

[2] F. Zhou, Y. Li, M. Xing, and Z. Bao, "An effective approach to ground moving target imaging and motion parameter estimation for single channel SAR system (in Chinese)," *Acta Electronica Sinica*, vol. 35, no. 3, pp. 543–548, 2007.

[3] Y. Chen, Y. Sun, and Q. Liu, "Parametric iterative soft thresholding algorithm for refocusing of moving targets in SAR images," *IEEE Trans. Geosci. Remote Sens.*, vol. 60, pp. 1–9, Jun. 2022, Art. no. 5229109.

[4] F. Zhou, R. Wu, M. Xing, and Z. Bao, "Approach for single channel SAR ground moving target imaging and motion parameter estimation," *IET Radar Sonar Navigation*, vol. 1, pp. 59–66, 2007.

[5] G. Li, X.-G. Xia, and Y.-N. Peng, "Doppler keystone transform: An approach suitable for parallel implementation of SAR moving target imaging," *IEEE Geosci. Remote Sens. Lett.*, vol. 5, no. 4, pp. 573–577, Oct. 2008.

[6] P. Huang, X.-G. Xia, Y. Gao, X. Liu, G. Liao, and X. Jiang, "Ground moving target refocusing in SAR imagery based on RFRT-FrFT," *IEEE Trans. Geosci. Remote Sens.*, vol. 57, no. 8, pp. 5476–5492, Aug. 2019.

[7] M. Çetin et al., "Sparsity-driven synthetic aperture radar imaging: Reconstruction, autofocusing, moving targets, and compressed sensing," *IEEE Signal Process. Mag.*, vol. 31, no. 4, pp. 27–40, Jul. 2014.

[8] J. A. Tropp and A. C. Gilbert, "Signal recovery from random measurements via orthogonal matching pursuit," *IEEE Trans. Inf. Theory*, vol. 53, no. 12, pp. 4655–4666, Dec. 2007.

[9] Y. Chen, G. Li, Q. Zhang, and J. Sun, "Refocusing of moving targets in SAR images via parametric sparse representation," *Remote Sens.*, vol. 9, no. 8, 2017, Art. no. 795.

[10] D. Wu, M. Yaghoobi, and M. E. Davies, "Sparsity-driven GMTI processing framework with multi-channel SAR," *IEEE Trans. Geosci. Remote Sens.*, vol. 57, no. 3, pp. 1434–1447, Mar. 2019.

[11] S. Zhang, Y. Liu, X. Li, and D. Hu, "Enhancing ISAR image efficiently via convolutional reweighted l1 minimization," *IEEE Trans. Image Process.*, vol. 30, pp. 4291–4304, 2021.

[12] S. Zhang, Y. Liu, and X. Li, "Micro-doppler effects removed sparse aperture ISAR imaging via low-rank and double sparsity constrained ADMM and linearized ADMM," *IEEE Trans. Image Process.*, vol. 30, pp. 4678–4690, Apr. 2021.

[13] S. Zhang, Y. Liu, and X. Li, "Computationally efficient sparse aperture ISAR autofocusing and imaging based on fast ADMM," *IEEE Trans. Geosci. Remote Sens.*, vol. 58, no. 12, pp. 8751–8765, Dec. 2020.

[14] X. Chen, C. Luo, Q. Yang, L. Yang, and H. Wang, "Efficient MMW image reconstruction algorithm based on ADMM framework for near-field MIMO-SAR," *IEEE Trans. Microw. Theory Techn.*, vol. 72, no. 2, pp. 1326–1338, Feb. 2024.

[15] X. Chen, Q. Yang, H. Wang, Y. Zeng, and B. Deng, "Adaptive ADMM-Based high-quality fast imaging algorithm for short-range MMW MIMO-SAR systems," *IEEE Trans. Antennas Propag.*, vol. 71, no. 11, pp. 8925–8935, Nov. 2023.

[16] S. Hao, Q. Zhang, and J. Sun, "Vibration compensation for airborne terahertz SAR imaging based on ADMM (in Chinese)," *J. Signal Process.*, vol. 39, no. 11, pp. 1933–1942, 2023.

[17] Y. Wang, Z. Wang, B. Zhao, and L. Xu, "Enhancement of azimuth focus performance in high-resolution SAR imaging based on the compensation for sensors platform vibration," *IEEE Sensors J.*, vol. 16, no. 16, pp. 6333–6345, Aug. 2016.

[18] B. Peng, X. Wei, B. Deng, H. Chen, Z. Liu, and X. Li, "A sinusoidal frequency modulation Fourier transform for radar-based vehicle vibration estimation," *IEEE Trans. Instrum. Meas.*, vol. 63, no. 9, pp. 2188–2199, Sep. 2014.

[19] Y. Li, Q. Wu, J. Wu, P. Li, Q. Zheng, and L. Ding, "Estimation of high-frequency vibration parameters for terahertz SAR imaging based on FrFT with combination of QML and RANSAC," *IEEE Access*, vol. 9, pp. 5485–5496, 2021.

[20] J. Cai, E. J. Candès, and Z. Shen, "A singular value thresholding algorithm for matrix completion," *SIAM J. Optim.*, vol. 20, no. 4, pp. 1956–1982, 2010.

[21] C. Lu, J. Feng, Y. Chen, W. Liu, Z. Lin, and S. Yan, "Tensor robust principal component analysis with a new tensor nuclear norm," *IEEE Trans. Pattern Anal. Mach. Intell.*, vol. 42, no. 4, pp. 925–938, Apr. 2020.

[22] D. Zhu, L. Wang, Y. Yu, Q. Tao, and Z. Zhu, "Robust ISAR range alignment via minimizing the entropy of the average range profile," *IEEE Geosci. Remote Sens. Lett.*, vol. 6, no. 2, pp. 204–208, Apr. 2009.

Xiaoyu Qin was born in Shandong, China, in 2000. She received the B.S. degree in Internet of Things engineering from Hunan Normal University, Changsha, China, in 2022. She is currently working toward the M.S. degree in information and communication engineering with the National University of Defense Technology, Changsha.

Her research interests include signal processing of radar and THz-SAR moving target imaging.

Bin Deng was born in Shandong, China, in 1980. He received the B.S. degree in communication engineering from Northeastern University, Shenyang, China, in 2004, and the M.S. and Ph.D. degrees in information and communication engineering from the National University of Defense Technology (NUDT), Changsha, China, in 2006 and 2011, respectively.

He is currently an Associate Professor with the College of Electronic Science and Technology, NUDT. His research interests include synthetic aperture radar (SAR), SAR/ground moving target indication, and terahertz radar.

Hongqiang Wang was born in Shaanxi, China, in 1970. He received the B.S. degree in information engineering, M.S., and Ph.D. degrees in information and communication engineering from the National University of Defense Technology (NUDT), Changsha, China, in 1993, 1999, and 2002, respectively.

Currently, he is a Professor with the College of Electronic Science and Technology, NUDT. He has been involved in modern radar signal processing research and development since 1996. His research interests include automatic target recognition, radar imaging, and target tracking.

Yang Zeng was born in Hunan, China, in 1989. He received the B.S. degree in optoelectronics engineering from the National University of Defense Technology, Changsha, China, in 2011, and the Ph.D. degree in electronic engineering from the Queen Mary University of London, London, U.K., in 2017.

His research interests include THz time-domain spectroscopy systems, quasi-optic measurements,and THz radar.

Xu Chen was born in Jilin, China, in 1995. He received the B.S. degree in civil engineering from Henan University, Zhengzhou, China, in 2017, and the M.S. degree in signal and information processing from Northeastern University, Shenyang, China, in 2020. He is currently working toward the Ph.D. degree in information and communication engineering with the National University of Defense Technology, Changsha, China.

His research interests include millimeter-wave radar imaging, radar waveform design, and signal processing.

Han Xiao was born in 1988. He received the B.S. degree in geographic information system from the China University of Geosciences, Beijing, China, in 2011, and the Ph.D. degree in photogrammetry and remote sensing from the Peking University, Beijing, in 2016.

His research interests include terahertz radar systems and signal processing of synthetic aperture radar.